

Ce Effects on Deformation-Induced Microstructure Evolution in Cu–Ti–Ni–Mg Alloys

Zhiyang Zhang, Meng Zhou,* Yi Zhang,* Shunlong Tang, Deye Xu, Baohong Tian, Xu Li, Yanlin Jia, Yong Liu, and Alex A. Volinsky

Cu–Ti–Ni–Mg and Cu–Ti–Ni–Mg–Ce alloys are prepared by vacuum induction melting. The hot deformation tests of the two alloys are carried out on the Gleeble-1500 simulator under the deformation temperatures of 550–950 °C and strain rates of 0.001–10 s⁻¹. The true stress–strain curves of the two alloys are obtained and the constitutive equations are established. The activation energy of the Cu–Ti–Ni–Mg alloy is 344.02 kJ mol⁻¹, and the activation energy of the Cu–Ti–Ni–Mg–Ce alloy is 389.87 kJ mol⁻¹. Based on the processing maps, the optimal processing parameters of the two alloys are obtained. The microstructure of the two alloys is analyzed by electron backscatter diffraction (EBSD) and transmission electron microscopy (TEM). The addition of Ce reduces the dislocation density and texture strength. The CuNi₂Ti precipitates are found in both alloys, and there are more precipitates in the Cu–Ti–Ni–Mg–Ce alloys. The addition of Ce increases the flow stress and activation energy, promotes precipitation, and improves the deformation resistance of the alloys.

1. Introduction

Currently, many applications require materials with high strength and electrical conductivity, and copper alloys are some of the better performing alloys. Due to their high strength and good electrical conductivity, copper alloys are widely used in lead frames, electronics, and other fields.^[1–5] In recent years, Cu–Ti alloys have attracted the attention of a wide range of researchers due to their excellent comprehensive properties. Cu–Ti alloys have high strength and hardness, good elasticity, wear resistance, workability, and stress relaxation resistance at high

temperatures.^[6–8] In addition, Cu–Ti alloys can be easily produced, they are nontoxic, meet the requirements of modern industrial development, and are potential alloys to replace Cu–Be alloys as conductive materials.^[9–11] Many researchers improved the properties of Cu–Ti alloys by adding alloying elements such as Cr, Zr, Al, Cd, Ni, Sn, and so on.^[12–17] Liu et al.^[18] investigated the effects of Ni addition on the microstructure and properties of Cu–Ti alloys by using the graded aging method. The results show that the addition of Ni generated a large amount of the Ni₃Ti phase, which reduced the content of solute titanium in the Cu matrix and improved the electrical conductivity of the alloy. After graded aging treatment at 300 °C for 2 h + 450 °C for 7 h, the conductivity and hardness of the Cu–3Ti–3Ni alloy can reach 31.34% IACS and 187 HV, respectively. Rouxel et al.^[19] investigated the addition of 0.3 wt% Fe to the Cu–6Ti alloy, and the results showed that the addition of Fe reduced the yield strength of the Cu–6Ti alloy from 521 to 323 MPa, while the elongation increased to 48%. Maki et al.^[20] found that a supersaturated solid solution of Mg in the Cu matrix resulted in high strength while maintaining the high electrical conductivity of the Cu alloy.

The addition of rare-earth elements significantly improves the properties of the alloy. Adding the right amount of rare-earth elements or compounds can improve plasticity, toughness, heat,

Z. Zhang, M. Zhou, Y. Zhang, S. Tang, D. Xu, B. Tian, Y. Liu
School of Materials Science and Engineering
Henan University of Science and Technology
Luoyang 471023, P. R. China
E-mail: zhoumeng@haust.edu.cn; yizhang@haust.edu.cn


M. Zhou, Y. Zhang, B. Tian, Y. Liu
Provincial and Ministerial Co-construction of Collaborative Innovation
Center for Non-ferrous Metals New Materials and Advanced Processing
Technology
Luoyang, Henan Province 471023, P. R. China

M. Zhou, Y. Zhang, B. Tian, Y. Liu
Henan Province Key Laboratory of Nonferrous Materials Science and
Processing Technology
Luoyang 471023, P. R. China

X. Li
Center for Advanced Measurement Science
National Institute of Metrology
Beijing 100029, P. R. China

Y. Jia
College of Materials Science and Engineering
Central South University
Changsha 410083, P. R. China

A. A. Volinsky
Department of Mechanical Engineering
University of South Florida
4202 E. Fowler Ave. ENG 030, Tampa, FL 33620, USA

 The ORCID identification number(s) for the author(s) of this article can be found under <https://doi.org/10.1002/adem.202201913>.

DOI: 10.1002/adem.202201913

and corrosion resistance.^[21] The incorporation of rare-earth elements into alloys has become a hot research topic in recent years. Stanford et al.^[22,23] investigated the effects of rare-earth elements addition on the alloy properties and showed that the addition of Ce leads to a decrease in the yield point of the alloy, while the ductility increases. Zhang et al.^[24] investigated the effects of Y addition on the microstructure of the Cu–Cr–Zr alloy during hot deformation, and the results showed that the addition of Y improved the flow stress, refined the grain, and promoted dynamic recrystallization.

Hot deformation of materials is widely used in manufacturing to improve the properties of alloys. The changes in temperature, strain rate, and microstructure during hot deformation are very important to optimize the hot deformation process. Choosing the most suitable deformation parameters can avoid cracks and holes and improve the quality of products. Therefore, in this paper, Cu–Ti–Ni–Mg and Cu–Ti–Ni–Mg–Ce alloys were prepared by adding Ni and Mg elements and the Ce trace element to the Cu–Ti alloy. The effects of the Ce addition on the microstructure and recrystallization behavior of the Cu–Ti–Ni–Mg alloy during hot deformation were investigated by hot deformation tests. The hot deformation temperature was 550–950 °C and the strain rate was 0.001–10 s⁻¹. The effects of Ce addition on the flow stress, microstructure evolution, and activation energy were compared. The precipitates in the Cu–Ti–Ni–Mg and Cu–Ti–Ni–Mg–Ce alloys were analyzed by transmission electron microscopy (TEM). The effects of Ce addition on dislocation density and texture changes were investigated by electron backscatter diffraction (EBSD). This study is important for the design, manufacturing, and thermomechanical processing of this high-performance copper alloy.

2. Experimental Section

The Cu–Ti–Ni–Mg and Cu–Ti–Ni–Mg–Ce alloys used in the experiment were cast in a ZG-0.01 vacuum frequency induction melting furnace. The experimental raw materials were 99% standard electrolytic cathode copper, pure Ni, Ti, Cu–30%Mg, and Cu–19% Ce alloys. In order to maintain the stability of the alloy composition and prevent the alloy from oxidizing, 0.05 MPa Ar gas was injected as a protective gas during smelting. The nominal and actual compositions of the Cu–Ti–Ni–Mg and Cu–Ti–Ni–Mg–Ce alloys are listed in **Table 1**. It can be seen that the nominal composition of the alloys differs somewhat from the tested composition because some Ni, Ti, and Mg are partially lost during the melting process. After melting, the alloy was poured into a sand mold with an inner diameter of 90 mm, an outer diameter of 170, and 190 mm high. After cooling, the ingot was annealed at 950 °C for 4 h, and after the riser was removed, it was cut into

Table 1. The nominal and analyzed composition of the alloys.

Alloy	Analyzed composition [wt%]				
	Ti	Ni	Mg	Ce	Cu
Cu–1Ti–1Ni–0.3Mg	0.906	0.906	0.31	–	Bal.
Cu–1Ti–1Ni–0.3Mg–0.1Ce	0.893	0.893	0.33	0.095	Bal.

Φ8 mm × 12 mm specimens for hot compression tests. After the specimens were processed, hot compression tests were performed using the Gleeble-1500 thermomechanical deformation simulator. Based on the phase diagram, the deformation temperature was set to 550–950 °C and the strain rate was 0.001–10 s⁻¹. First, the heating rate was set to 10 °C s⁻¹, and the specimens were heated to the corresponding individual temperature, and then held at constant temperature for 3 min, followed by the hot compression test. In the hot compression test, the specimens were deformed to 55% compression.

After the hot compression experiments, the specimens were cut along the compression direction and the microstructure changes of the Cu–Ti–Ni–Mg and Cu–Ti–Ni–Mg–Ce alloys were observed by JSM-7800F field emission scanning electron microscope and FEI Tecnai F30 transmission electron microscope. Samples for EBSD observations were first coarsely ground with different sandpaper, then finely polished with a polisher, and finally electro-polished for 1 min. The composition of the electrolyte is 50% phosphoric acid and 50% alcohol. EBSD images were obtained using a JSM-7800F field emission scanning electron microscope with a step size of 2.5 μm operated at 20 kV. Specimens for TEM analysis were first mechanically polished to 70 μm thickness, 3 mm diameter discs, and then ion milled using Gatan 691. It is important to note that EBSD and TEM samples were stored in a vacuum to prevent contamination.

3. Results and Discussion

3.1. True Stress–True Strain Curves

The true stress–true strain curves of the Cu–Ti–Ni–Mg and Cu–Ti–Ni–Mg–Ce alloys obtained at different temperatures and strain rates are shown in **Figure 1**. During hot deformation, the changes in the true stress–true strain curves are mainly caused by superimposed changes in work hardening, dynamic recovery, and dynamic recrystallization (DRX).^[25] The entire hot deformation process is mainly divided into three stages. In the first stage, the flow stress rises rapidly, which is a typical feature of work hardening. During the work hardening stage, a large number of dislocations are generated, the density of dislocations increases dramatically, and the dislocations become entangled with each other. As a result, the dislocation motion is impeded, leading to a significant increase in flow stress.^[26,27] In the second stage, the flow stress rises slowly until it reaches a peak value, and the true stresses gradually plateau. At this stage, the dynamic recovery of softening mechanism begins to appear, which means that the dislocations cancel each other out through slip and adhesion, resulting in the decrease of dislocation density. When the proliferation and consumption of dislocations reach equilibrium, the flow stress is in equilibrium. In the third stage, the flow stress decreases continuously. With the continuous increase of strain, the dynamic recrystallization ability begins to strengthen, and the dynamic recovery and dynamic recrystallization effects are greater than work hardening and occupy a dominant position so that the flow stress continues to decrease.

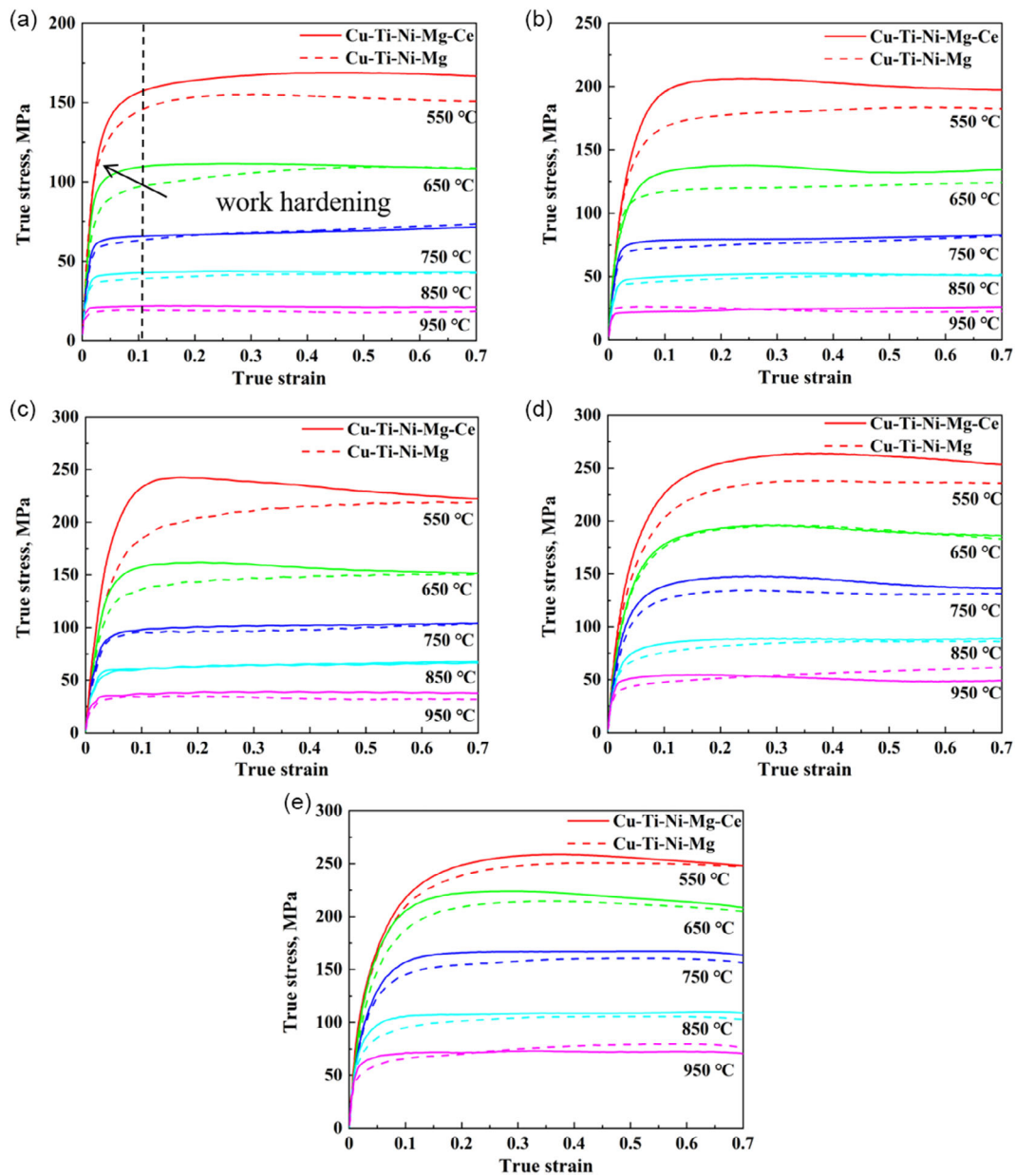


Figure 1. The true stress–true strain curves of the Cu–Ti–Ni–Mg and Cu–Ti–Ni–Mg–Ce alloys deformed at different temperatures and strain rates: a) 0.001 s^{-1} , b) 0.01 s^{-1} , c) 0.1 s^{-1} , d) 1 s^{-1} , and e) 10 s^{-1} .

It can be seen from Figure 1 that temperature and strain rate significantly affect the flow stress. For example, as shown in Figure 1a, at a strain rate of 0.001 s^{-1} , the peak stress of the Cu–Ti–Ni–Mg alloy decreased from 155 to 109 MPa when the temperature was increased from 550 to 650 °C. Under the same conditions, the peak stress of the Cu–Ti–Ni–Mg–Ce alloy decreased from 169 to 118 MPa. This is due to the increased average kinetic energy of the atoms with temperature, which promotes the diffusion of metal atoms in the alloy, together with the large number of dislocations that proliferate during hot deformation, thus increasing the dynamic softening capacity of the alloy. In addition, as shown

in Figure 1c,d, when the deformation temperature is 750 °C, the peak stress of the Cu–Ti–Ni–Mg alloy increases from 84 to 105 MPa with the strain rate change from 0.01 to 0.1 s^{-1} . With the increase in strain rate, a large number of dislocations are generated within the alloy in a short time, and the probability of entanglement and intersection among the dislocations increases, which leads to the blockage of their movement, and thus produces a more obvious work hardening effect. Therefore, it can be concluded that the flow stress gradually rises with the decrease in temperature and the increase in strain rate. This may explain why dynamic recrystallization is easier at higher temperatures or lower strain rates.

Compared with the Cu–Ti–Ni–Mg alloy, the flow stress of the Cu–Ti–Ni–Mg–Ce alloy is significantly higher at the same deformation temperature and strain rate. The addition of Ce can promote precipitation, and finally increase the flow stress of the alloy through the pinning effect of the precipitation phase. This phenomenon can be confirmed by the TEM results.

3.2. Constitutive Equations

During hot processing, the activation energy is an energy threshold that needs to be crossed by the metal atoms as the alloy undergoes plastic deformation.^[28,29] It is an important parameter to evaluate the hot workability of alloys. In order to obtain the thermal activation energy of the alloy, the constitutive equations of the Cu–Ti–Ni–Mg and Cu–Ti–Ni–Mg–Ce alloys were established based on the flow stress data. The purpose of constitutive equations is to describe the relationship between the flow stress, hot deformation temperature, and strain rate. The constitutive equation proposed by Sellars and McTegart is widely used to describe the relationship between the peak stress, deformation temperature, and strain rate in the process of hot deformation.^[30] It can be expressed as

$$\dot{\epsilon} = A_1 \left[\sigma^{n_1} \exp \left[-\frac{Q}{RT} \right] \right] \alpha\sigma < 0.8 \quad (1)$$

$$\dot{\epsilon} = A_2 \left[(\beta\sigma) \exp \left[-\frac{Q}{RT} \right] \right] \alpha\sigma > 1.2 \quad (2)$$

$$\dot{\epsilon} = A \left[\sinh(\alpha\sigma)^n \exp \left[-\frac{Q}{RT} \right] \right] \text{(For all)} \quad (3)$$

Here, A , A_1 , A_2 , α , n , and n_1 are the material constants, $\dot{\epsilon}$ is the strain rate, T is the deformation temperature in K, and σ is the peak stress. Q is the activation energy and R is the universal gas constant ($R = 8.314 \text{ J mol}^{-1}\text{K}$).

The Zener–Hollomon parameter $Z^{[31,32]}$ is used to represent the influence of temperature and deformation rate on the flow stress

$$Z = A[\sinh(\alpha\sigma)]^n = \dot{\epsilon} \exp \left[\frac{Q}{RT} \right] \quad (4)$$

Taking the natural logarithm of both sides of Equation (1–3) yields

$$\ln \dot{\epsilon} = n_1 \ln \sigma + \ln A_1 - \frac{Q}{RT} \quad (5)$$

$$\ln \dot{\epsilon} = \beta \sigma + \ln A_2 - \frac{Q}{RT} \quad (6)$$

$$\ln \dot{\epsilon} = n \ln[\sinh(\alpha\sigma)] - \frac{Q}{RT} + \ln A \quad (7)$$

According to calculations, $n_1 = 11.333$, $\beta = 0.1067$, and $\alpha = \beta/n_1 = 0.0094$ for Cu–Ti–Ni–Mg as an example. n is the average of the slopes of $\ln \dot{\epsilon}$ and $\ln[\sinh(\alpha\sigma)]$ in Figure 4c, $n = 7.7187$. The activation energy (Q) is then defined as

$$Q = R \left[\frac{\partial(\ln \dot{\epsilon})}{\partial \ln[\sinh(\alpha\sigma)]} \right]_{\text{T}} \left[\frac{\partial \ln[\sinh(\alpha\sigma)]}{\partial(1/T)} \right]_{\dot{\epsilon}} = RnS \quad (8)$$

Here, S is the average of the slope of $\ln[\sinh(\alpha\sigma)] - T^{-1}/10^{-3} \text{ K}^{-1}$ in Figure 2d, and $S = 5.3608 \text{ K}$. Bringing the relevant data into Equation (8), the average activation energy of Cu–Ti–Ni–Mg is $343.8 \text{ kJ mol}^{-1}$. Figure 2e shows the linear relationship between $\ln Z$ and $\ln[\sinh(\alpha\sigma)]$. The relevant relationship is

$$\ln Z = \ln A + n[\ln[\sinh(\alpha\sigma)]] \quad (9)$$

$\ln A$ is the intercept in Figure 2e, which is $\ln A = 37.35$. Therefore, the value of A can be calculated as $A = e^{37.35}$. According to the above values, the constitutive equation of the Cu–Ti–Ni–Mg alloy can be expressed as

$$\dot{\epsilon} = e^{37.35} [\sinh(0.0094\sigma)]^{7.72} \exp \left(-\frac{344020}{8.314T} \right) \quad (10)$$

In the same way, the constitutive equation of the Cu–Ti–Ni–Mg–Ce alloy is

$$\dot{\epsilon} = e^{40.92} [\sinh(0.0092\sigma)]^{7.94} \exp \left(-\frac{389870}{8.314T} \right) \quad (11)$$

The activation energy of the Cu–Ti–Ni–Mg and Cu–Ti–Ni–Mg–Ce alloys is 344.02 and $389.87 \text{ kJ mol}^{-1}$, respectively. Figure 2f is a comparison of the activation energy of pure Cu,^[33] Cu–Ti–Ni–Mg, and Cu–Ti–Ni–Mg–Ce alloys. The self-diffusion activation energy of pure copper is $203.6 \text{ kJ mol}^{-1}$, while the activation energy of Cu–Ti–Ni–Mg and Cu–Ti–Ni–Mg–Ce alloys is higher than pure copper. The presence of more precipitated phases in both alloys inhibits dislocation movement and thus enhances the deformation resistance of the alloys. Therefore, the two alloys have a higher activation energy and show better high-temperature stability.

It can be seen from Figure 2f that with the addition of Ce, the activation energy of the Cu–Ti–Ni–Mg alloy is increased by about 13%. The main reason is that the addition of Ce promotes precipitation, purifies the copper matrix, and the precipitated phase has a smaller size and more uniform distribution. The precipitation hinders the movement of dislocations and grain boundaries in the hot deformation motion by pinning them, which leads to difficulties in dislocation movement and requires more energy to overcome the obstacles, so the addition of Ce increases the activation energy.

3.3. Processing Maps

The establishment of a hot processing map can effectively predict the hot processing properties of metals and is an important part of determining the material process parameters. The unstable regions during plastic deformation can be avoided and stable regions can be obtained from the hot processing map.^[34] According to the material model theory of dynamic materials, the total power in plastic deformation P consists of the dissipation caused by plastic deformation G and the dissipation related to the microstructure evolution J , and the total power P can be described as

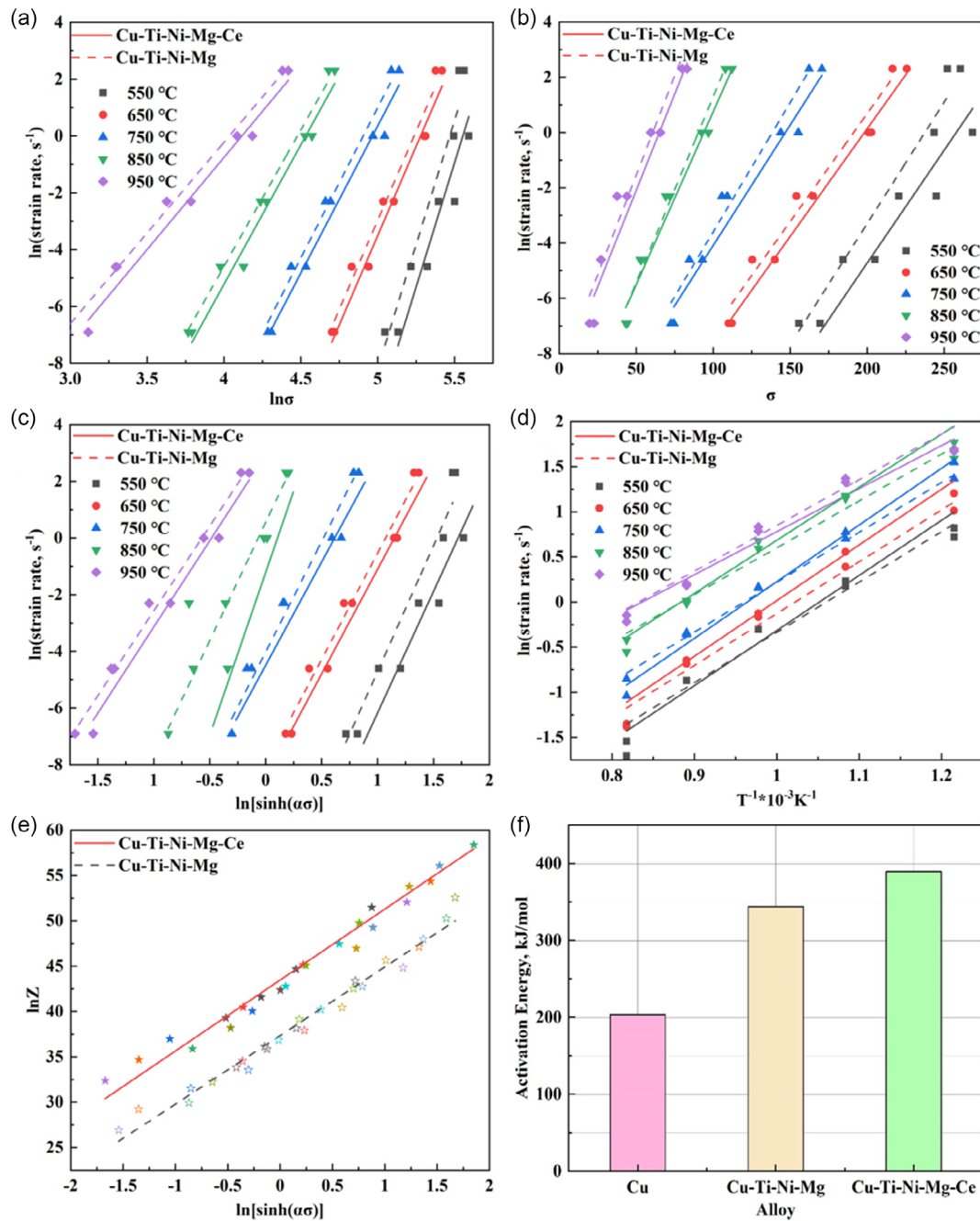


Figure 2. Relationships between: a) $\ln(\text{strain rate})$ and $\ln \sigma$, b) $\ln(\text{strain rate})$ and σ , c) $\ln(\text{strain rate})$ and $\ln[\sinh(\alpha\sigma)]$, d) $\ln[\sinh(\alpha\sigma)]$ and $T^{-1}/10^{-3} \text{K}^{-1}$, e) $\ln Z$ and $\ln[\sinh(\alpha\sigma)]$, f) activation energy of Cu, Cu-Ti-Ni-Mg, and Cu-Ti-Ni-Mg-Ce alloys.

$$P = \delta \dot{\epsilon} = G + J = \int_0^{\dot{\epsilon}} \sigma d\dot{\epsilon} + \int_0^{\sigma} \dot{\epsilon} d\sigma \quad (12)$$

Here, $\dot{\epsilon}$ is the strain rate and σ is the flow stress. During hot processing, the proportion of power absorbed by deforming the material is called the power dissipation efficiency η , which is defined as

$$\eta = \frac{2m}{m+1} \quad (13)$$

Here, m is the strain rate sensitivity parameter, which represents the relationship between G and J at constant temperature and strain

$$m = \frac{\partial J}{\partial G} = \frac{\partial \ln \sigma}{\partial \ln \dot{\epsilon}} \quad (14)$$

The parameter η varies with the deformation temperature and the strain rate, and the power dissipation scatter diagram can be obtained according to the η value under different conditions. The power dissipation map shows areas with the highest power efficiency. The higher the η value, the better the workability. At the same time, according to the flow instability criterion,^[35] the unstable region of the alloy can be determined as

$$\xi(\dot{\epsilon}) = \frac{\partial \ln \left(\frac{m}{m+1} \right)}{\partial \ln \dot{\epsilon}} + m < 0 \quad (15)$$

When $\xi(\dot{\epsilon}) < 0$, the material will be unstable. However, the unstable regions may lead to adiabatic deformation zones, holes, cracks, and so on.^[36] The instability map consists of the instability parameter $\xi(\dot{\epsilon})$, temperature T , and the strain rate $\dot{\epsilon}$. The instability map is superimposed on the power dissipation map to construct the processing map.

Figure 3 shows the processing maps for the Cu–Ti–Ni–Mg and Cu–Ti–Ni–Mg–Ce alloys at strains of 0.1 and 0.5. The values in the maps represent the maximum power consumption efficiency, and the higher the value, the better the workability

performance of the alloy. The colored and shaded areas correspond to the stable and unstable regions, respectively. A_1 , A_2 , B_1 , and B_2 represent the optimal processing domain for the two alloys at strains of 0.1 and 0.5, respectively. The optimal processing domain of the Cu–Ti–Ni–Mg alloy is at 825–950 °C and 0.012–0.162 s⁻¹ strain rate. The optimal processing domain of the Cu–Ti–Ni–Mg–Ce alloy is at 725–950 °C and 0.015–0.185 s⁻¹ strain rate. Therefore, the addition of Ce improved the optimal processing domain, which made the Cu–Ti–Ni–Mg alloy more suitable for processing. The unstable regions of both alloys are at the high strain rate of 0.11–10 s⁻¹. At high strain rates, the deformation time is short and the grain boundaries do not have time to slide, resulting in stress concentrations at the dislocation pile-up. The stress concentration is difficult to be released in a short time and may lead to the fracture of the specimen. Therefore, one should avoid unstable areas when designing the hot working process of the alloy.

3.3.1. EBSD Analysis

Electron backscatter diffraction is used to analyze the texture, grain size, and orientation of the alloy.^[37] Figure 4a,b shows the inverse pole figure (IPF) maps of the Cu–Ti–Ni–Mg alloy deformed at 750 and 850 °C with 0.001 s⁻¹ strain rate. It can

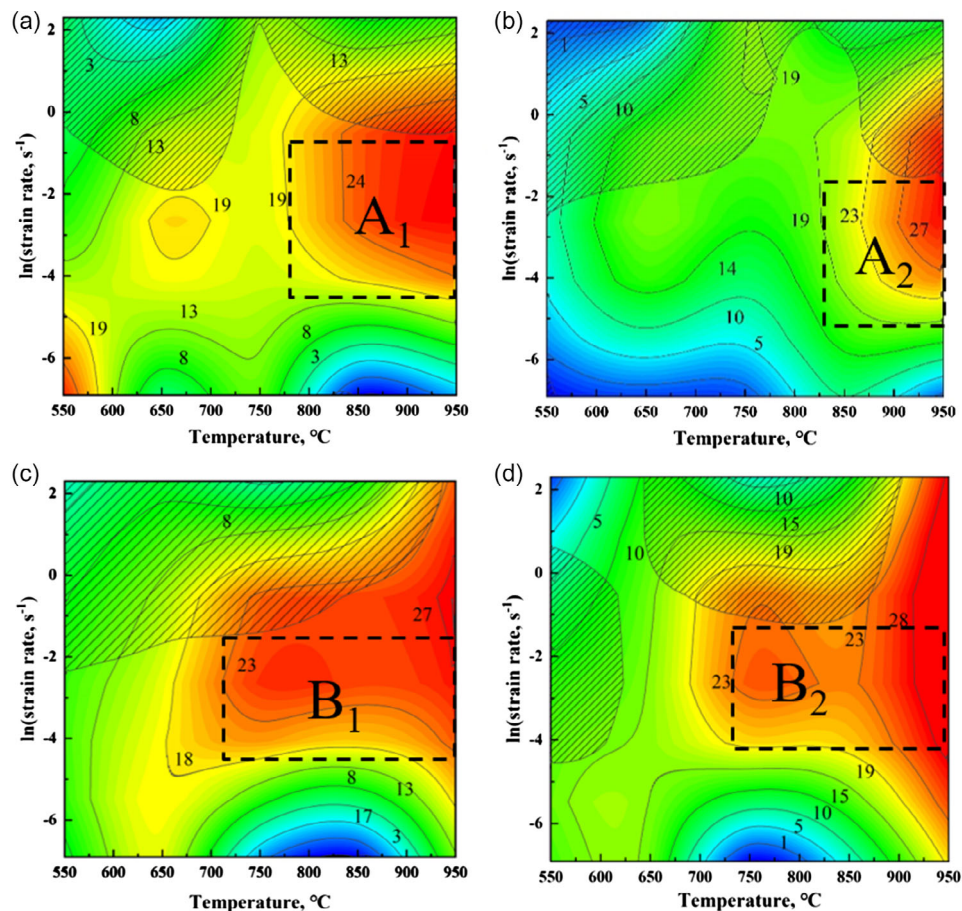


Figure 3. Processing maps under different strains. Cu–Ti–Ni–Mg alloy: a) $\epsilon = 0.1$, b) $\epsilon = 0.5$; Cu–Ti–Ni–Mg–Ce alloy: c) $\epsilon = 0.1$, d) $\epsilon = 0.5$. The shaded areas represent unstable regions.

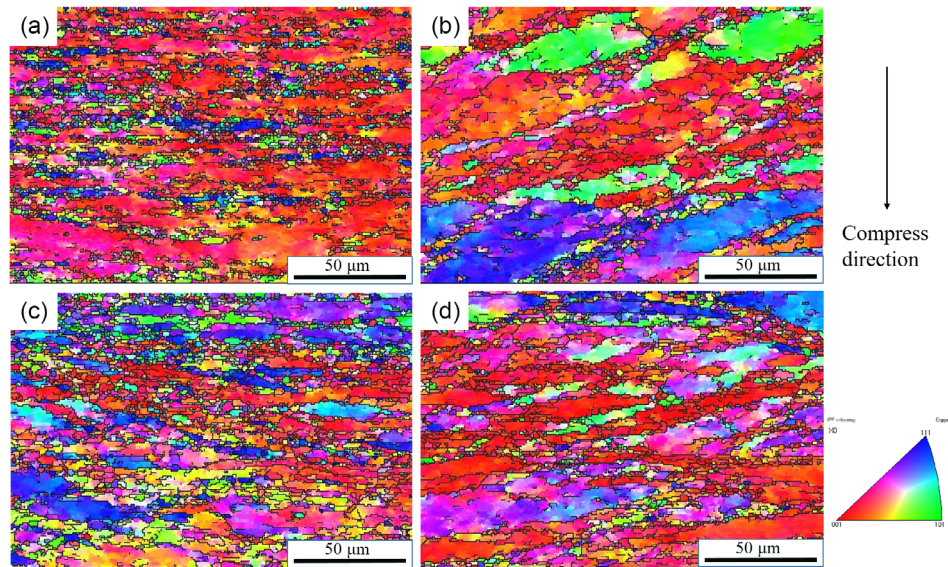


Figure 4. EBSD images of alloys deformed at 0.001 s^{-1} strain rate and different temperatures: a) Cu-Ti-Ni-Mg at $750 \text{ }^\circ\text{C}$, b) Cu-Ti-Ni-Mg at $850 \text{ }^\circ\text{C}$, c) Cu-Ti-Ni-Mg-Ce at $750 \text{ }^\circ\text{C}$, d) Cu-Ti-Ni-Mg-Ce at $850 \text{ }^\circ\text{C}$.

be seen from Figure 4a,b that the hot compression elongates the grains. In addition, at the edge of the coarsely deformed grains, recrystallized grains begin to appear. This is because the grain boundary is more conducive to DRX growth.^[38] As the temperature increases, the recrystallized grains gradually replace the deformed grains. At the same time, as the temperature continues to rise, the new recrystallized grains grow gradually, making the grain size larger. Figure 4c,d shows the EBSD images of the Cu-Ti-Ni-Mg-Ce alloy deformed at 750 and $850 \text{ }^\circ\text{C}$ with 0.001 s^{-1} strain rate. When the temperature rises from 750 to $850 \text{ }^\circ\text{C}$, the increase in temperature provides the driving force for the nucleation and growth of DRX, so the DRX grains grow gradually, engulfing and replacing the original deformed grains. This indicates that recrystallization is promoted by temperature increase. At higher temperatures, the DRX grain size is larger, which is typical DRX behavior.^[39] Under the same conditions, the grain size of the Cu-Ti-Ni-Mg-Ce alloy is smaller than the Cu-Ti-Ni-Mg alloy, and the DRX grains of the Cu-Ti-Ni-Mg-Ce alloy are larger. These results show that the addition of Ce promotes the nucleation and growth of DRX and increases the deformation resistance of the alloy.

Figure 5 shows the dynamic recrystallization distribution of the Cu-Ti-Ni-Mg and Cu-Ti-Ni-Mg-Ce alloys deformed at 0.001 s^{-1} strain rate and different deformation temperatures. The volume fraction of dynamic recrystallization of the Cu-Ti-Ni-Mg alloy increased from 13.7% to 14.4% when the temperature was increased from 750 to $850 \text{ }^\circ\text{C}$, indicating that the temperature increase promoted recrystallization. Comparing Figure 5a,c, the dynamic recrystallization volume fraction of the Cu-Ti-Ni-Mg-Ce alloy is 21.6% , and the Cu-Ti-Ni-Mg alloy is 13.7% under the same conditions, which proves that the addition of Ce promotes dynamic recrystallization.

Figure 6 shows the misorientation angle distribution of the Cu-Ti-Ni-Mg and Cu-Ti-Ni-Mg-Ce alloys deformed at

different temperatures and 0.001 s^{-1} strain rate. It can be seen from Figure 6 that the misorientation angles of the Cu-Ti-Ni-Mg and Cu-Ti-Ni-Mg-Ce alloys have a large aggregation at the low-angle grain boundaries (LAGBs, angle $< 15^\circ$), which are associated with stored dislocations and also lead to the creation of work-hardened regions.^[40] As shown in Figure 6a,b, the percentage of high-angle grain boundaries (HAGBs, angle $> 15^\circ$) of the Cu-Ti-Ni-Mg alloy increased from 22.7% to 31.2% with deformation temperature. The percentage of HAGBs in the Cu-Ti-Ni-Mg-Ce alloy increased from 27.9% to 35.1% , as shown in Figure 6c,d. Because the migration rate of HAGBs is faster than small-angle grain boundaries, high temperature will promote the migration of HAGBs, thereby consuming dislocations in the path. In addition, the growth and coarsening of dynamic recrystallization also transformed the small-angle grain boundaries into HAGBs, so the proportion of HAGBs increased with temperature. Comparing Figure 6a,c, there are more HAGBs in the Cu-Ti-Ni-Mg-Ce alloy than in the Cu-Ti-Ni-Mg alloy under the same deformation conditions, indicating that the addition of Ce increases the proportion of HAGBs, accelerates the dislocation consumption, and promotes the recrystallization growth.

The migration rate of grain boundaries is closely related to the dislocations near the grain boundaries, which also affects the dynamic recrystallization of the alloy.^[27] The geometrically necessary dislocation (GND) density is related to the kernel average misorientation (KAM) and can be expressed as^[41,42]

$$\rho^{\text{GND}} = \frac{2\theta}{\mu b} \quad (16)$$

Here, ρ^{GND} is the GND density in m^{-2} and θ is the average local misorientation angle in radians. μ represents the step size of the scan in μm , and b is the Burger's vector of 0.255 nm . In this

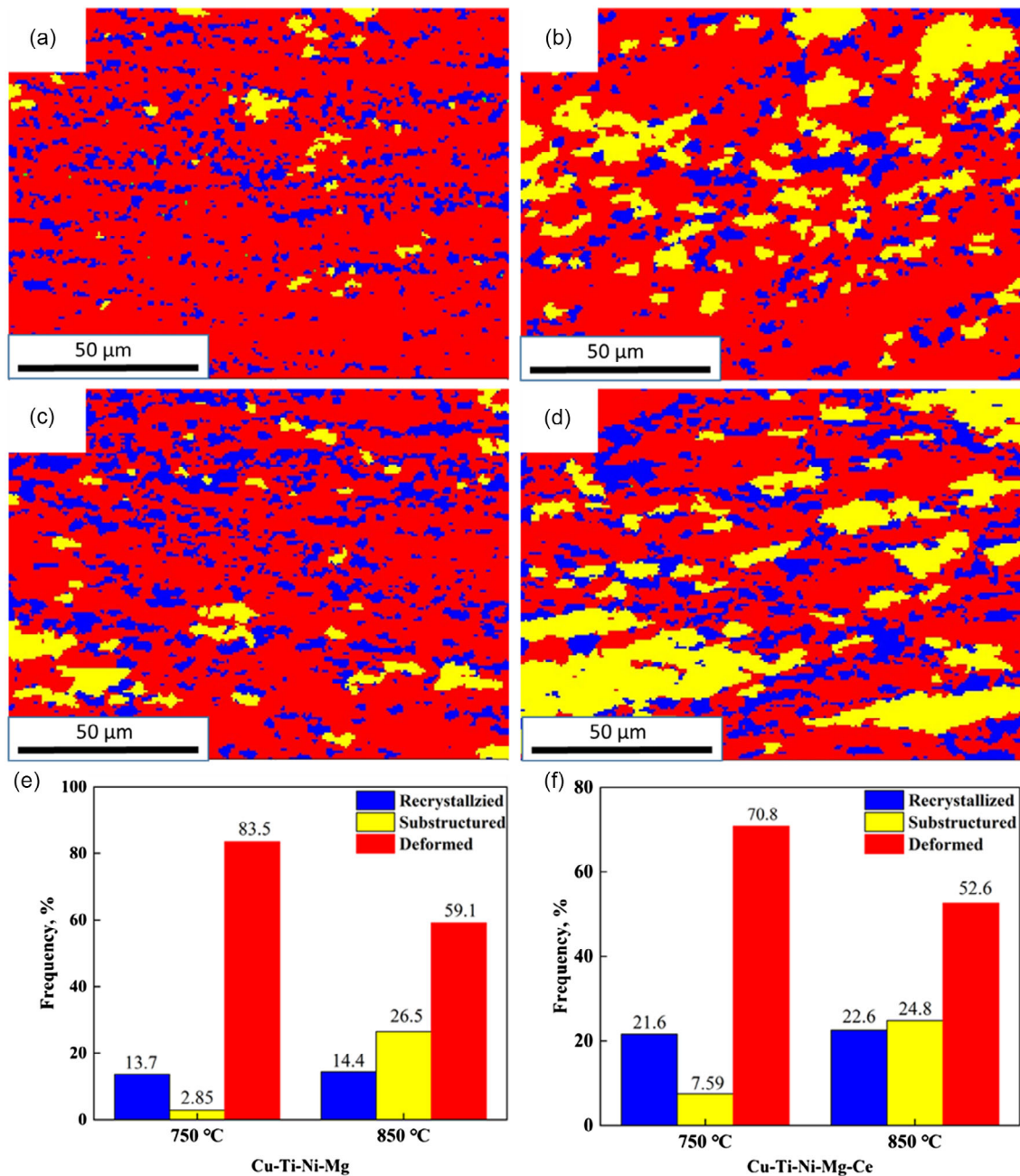


Figure 5. Dynamic recrystallization distribution of the Cu-Ti-Ni-Mg and Cu-Ti-Ni-Mg-Ce alloys deformed at 0.001 s^{-1} strain rate and different temperatures: a) Cu-Ti-Ni-Mg at 750 °C, b) Cu-Ti-Ni-Mg at 850 °C, c) Cu-Ti-Ni-Mg-Ce at 750 °C, d) Cu-Ti-Ni-Mg-Ce at 850 °C, e) grain type frequency of Cu-Ti-Ni-Mg, and f) grain type frequency of Cu-Ti-Ni-Mg-Ce.

article, the critical angle is defined as 3° and misorientation angles greater than 3° are excluded from the calculation.

Figure 7 shows the KAM of the Cu-Ti-Ni-Mg and Cu-Ti-Ni-Mg-Ce alloys deformed at 0.001 s^{-1} strain rate, 750 °C, and 850 °C. As shown in Figure 7a,b, the dislocation density of the Cu-Ti-Ni-Mg alloy deformed at 750 and 850 °C is 4.5×10^{16} and $4.1 \times 10^{16} \text{ m}^{-2}$, respectively. The results show that the value of ρ^{GND} decreases when the temperature increases from 750 to

850 °C, and the energy required for the recrystallization process is usually provided by dissipating dislocations, so this also proves that the temperature promotes dynamic recrystallization. Similarly, it can be seen from Figure 7c,d that the Cu-Ti-Ni-Mg-Ce alloy has the same phenomenon under the same deformation conditions. Comparing Figure 7a,c, the ρ^{GND} value of the Cu-Ti-Ni-Mg-Ce alloy is lower than the Cu-Ti-Ni-Mg alloy, which indicates that the addition of Ce increases the dislocation

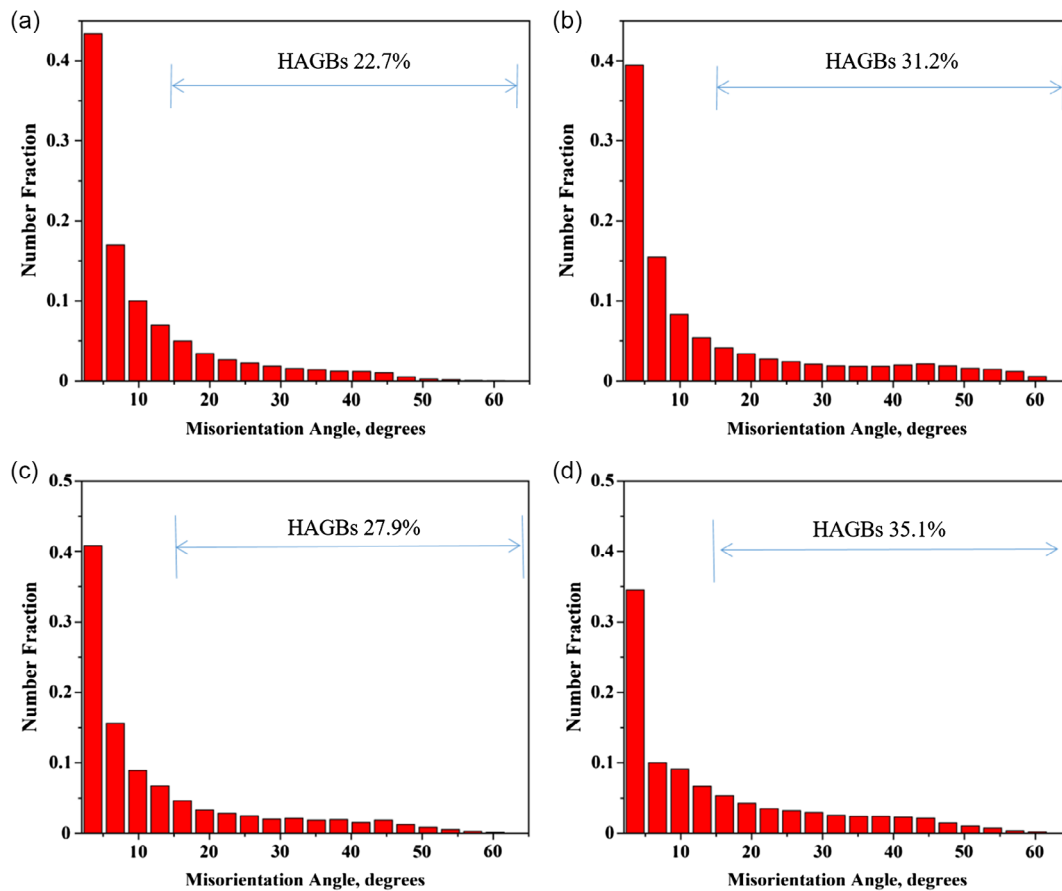


Figure 6. EBSD misorientation angle distribution in the Cu-Ti-Ni-Mg and Cu-Ti-Ni-Mg-Ce alloys deformed at 0.001 s^{-1} strain rate and different deformation temperatures: a) Cu-Ti-Ni-Mg at $750\text{ }^{\circ}\text{C}$, b) Cu-Ti-Ni-Mg at $850\text{ }^{\circ}\text{C}$, c) Cu-Ti-Ni-Mg-Ce at $750\text{ }^{\circ}\text{C}$, and d) Cu-Ti-Ni-Mg-Ce at $850\text{ }^{\circ}\text{C}$.

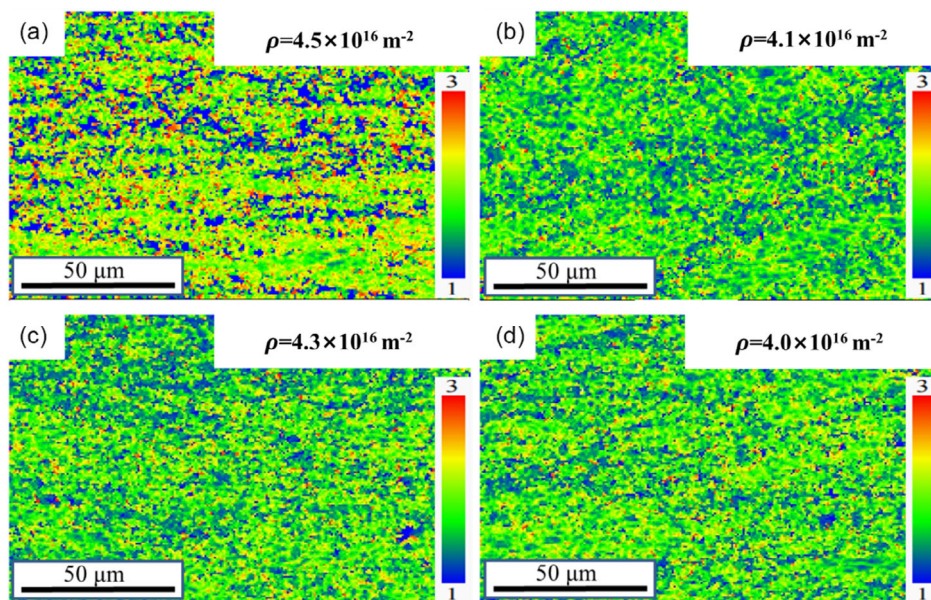


Figure 7. The KAM maps of alloys deformed at 0.001 s^{-1} strain rate and different temperatures: a) Cu-Ti-Ni-Mg at $750\text{ }^{\circ}\text{C}$, b) Cu-Ti-Ni-Mg at $850\text{ }^{\circ}\text{C}$, c) Cu-Ti-Ni-Mg-Ce at $750\text{ }^{\circ}\text{C}$, and d) Cu-Ti-Ni-Mg-Ce at $850\text{ }^{\circ}\text{C}$.

consumption and provides more driving force for the recrystallization to proceed, promoting the dynamic recrystallization process of the alloy.

In order to study the recrystallization texture evolution of the Cu–Ti–Ni–Mg and Cu–Ti–Ni–Mg–Ce alloys during hot deformation, the inverse pole figures were obtained, as shown in Figure 8 and 9. Figure 8 shows the inverse pole figures of the Cu–Ti–Ni–Mg alloy deformed at 750 and 850 °C with 0.001 s⁻¹ strain rate. By comparing standard inverse polar figures, the main fiber texture of the Cu–Ti–Ni–Mg alloy deformed at 750 °C is <110>||X and <111>||X, and the main fiber texture of the alloy deformed at 850 °C is <100>||X. Figure 9 shows the inverse pole figures of the Cu–Ti–Ni–Mg–Ce alloy deformed at 750 and 850 °C with 0.001 s⁻¹ strain rate. The main fiber texture of the Cu–Ti–Ni–Mg–Ce alloy deformed at 750 °C is <100>||X and <111>||X, and the main fiber texture of the alloy deformed at 850 °C is <100>||X and <110>||X. By comparing

Figure 8 and 9, the maximum texture strength decreases from 3.614 to 2.56 with the addition of Ce. The results show that the addition of rare earth Ce reduces the texture strength of the alloy.

3.4. TEM Analysis

Many studies have shown that the addition of rare-earth elements can promote precipitation.^[43] To study the influence of adding Ce to Cu–Ti–Ni–Mg alloys on precipitation during hot deformation, FEI Tecnai F30 transmission electron microscope was used to analyze the microstructure of the alloys deformed at a strain rate of 0.001 s⁻¹ and 750 °C. Figure 10 shows the microstructure of the Cu–Ti–Ni–Mg alloy deformed at 0.001 s⁻¹ strain rate and 750 °C. It can be seen from Figure 10a that there are many uniformly distributed nanosized precipitated phases and dislocations in the copper matrix. Figure 10b is the bright field

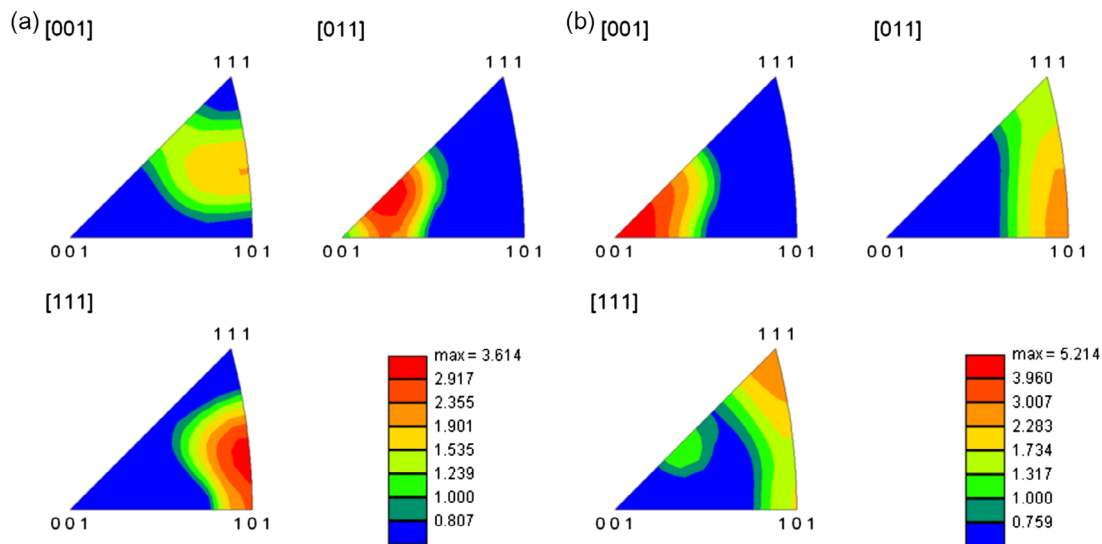


Figure 8. Inverse pole figures of the Cu–Ti–Ni–Mg alloy deformed at 0.001 s⁻¹ strain rate and different temperatures: a) 750 °C; b) 850 °C.

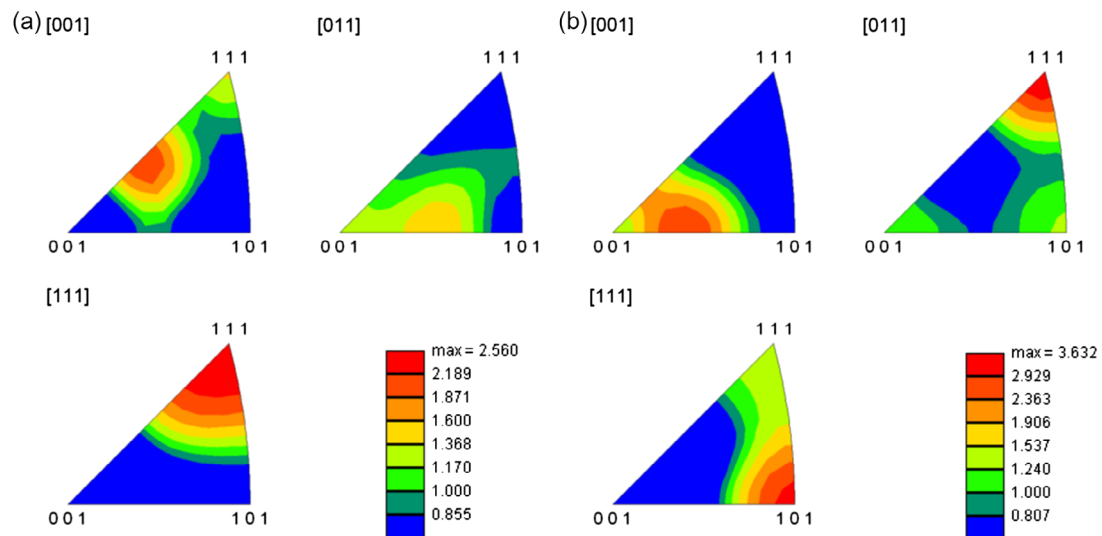


Figure 9. Inverse pole figures of the Cu–Ti–Ni–Mg–Ce alloy deformed at 0.001 s⁻¹ strain rate and different temperatures: a) 750 °C; b) 850 °C.

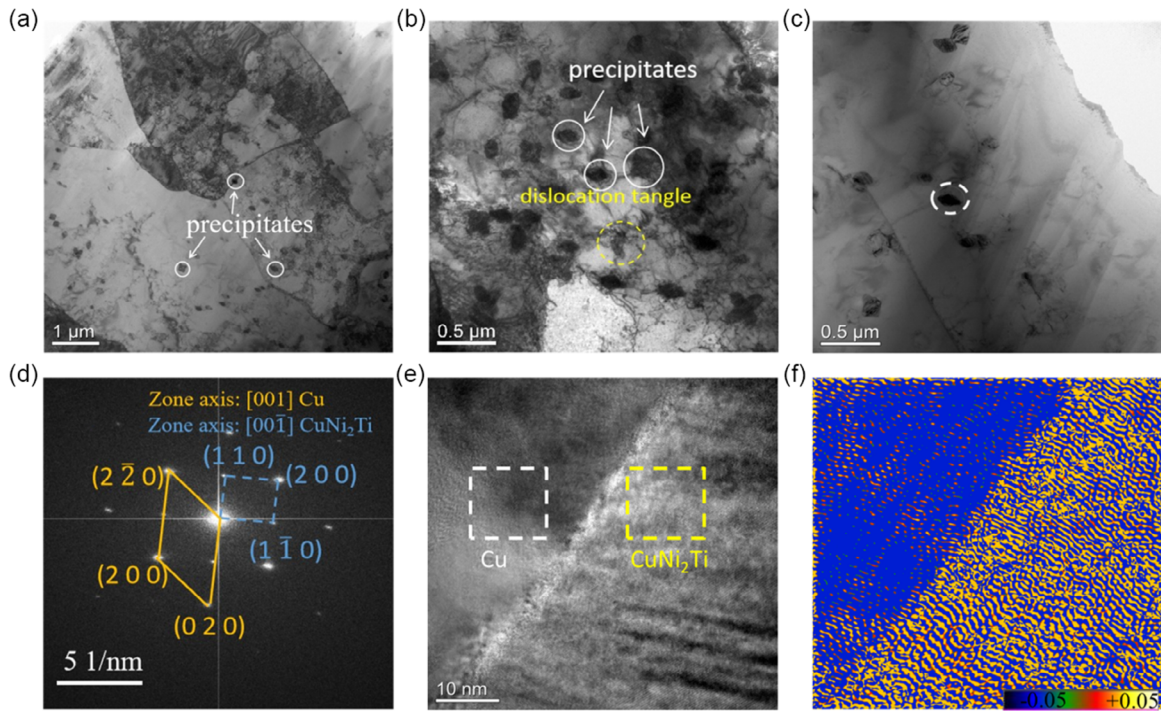


Figure 10. TEM images of the Cu-Ti-Ni-Mg alloy deformed at 750 °C and 0.001 s⁻¹ strain rate: a, b) bright-field micrographs, c) precipitates, d) SADP, e) corresponding HRTEM, and f) GPA of (e).

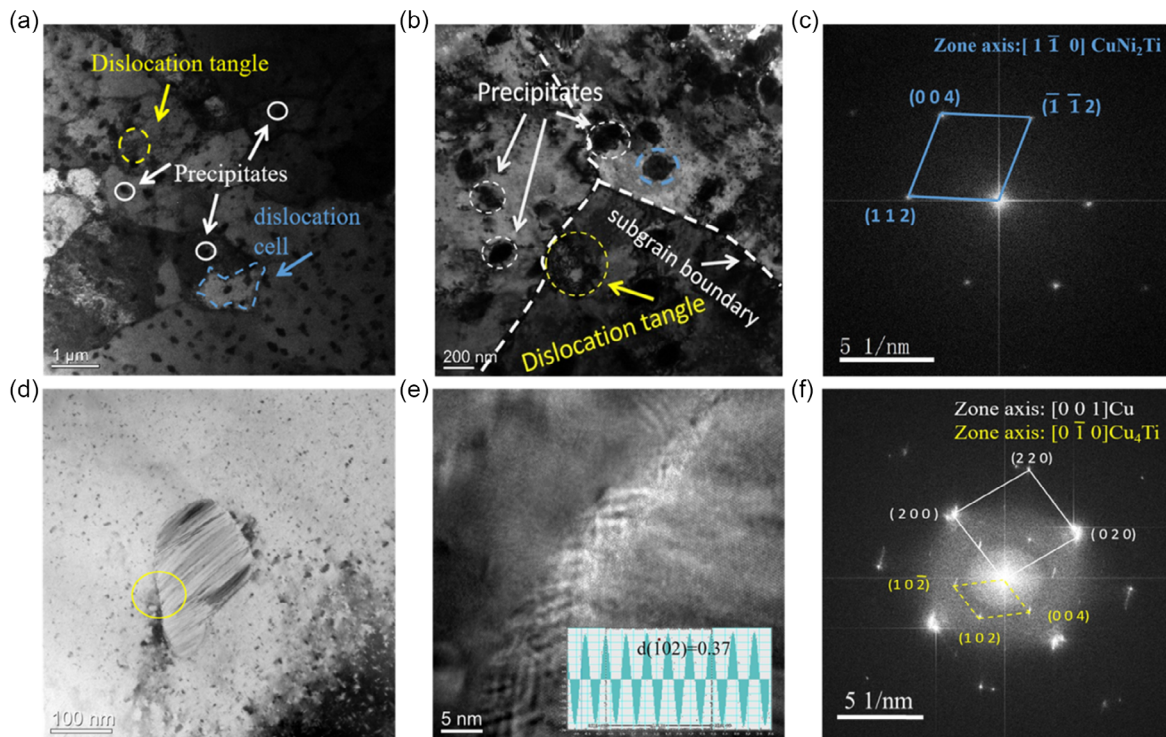


Figure 11. TEM images of the Cu-Ti-Ni-Mg-Ce alloy deformed at 750 °C and 0.001 s⁻¹ strain rate: a, b) bright-field images, c) CuNi₂Ti SADP, d) precipitate, e) HRTEM of the precipitate, and f) FFT corresponding to (e).

image of the precipitated phase with many dislocations around the precipitated phase. The dislocations interact with the precipitation to form dislocation entanglements, which hinder the movement of dislocations. In Figure 10c, the ellipsoidal precipitated phase is marked by circles, which is uniformly present in the matrix with a length between 200 and 300 nm. Figure 10d shows the small area diffraction pattern (SADP) corresponding to the precipitation. Based on the calibration results, the precipitates are identified as CuNi_2Ti with an orthorhombic structure and lattice parameters $a = 0.361$ nm, $b = 0.361$ nm, and $c = 7.459$ nm. The zone axes of Cu and CuNi_2Ti are $[001]_{\text{Cu}}$ and $[00\bar{1}]_{\text{CuNi}_2\text{Ti}}$, respectively. Figure 10e shows the HRTEM corresponding to the precipitation, with the copper matrix on the left and the precipitation on the right. Figure 10f is the geometric phase analysis (GPA) of Figure 10e. According to the color scheme, it can be seen that there is compressive stress in most copper phases and tensile stress in CuNi_2Ti with uniform strains. The lattice distortion of the copper phase and CuNi_2Ti phase plays an important role in the enhancement of Cu–Ti–Ni–Mg alloy properties.

Figure 11 shows the microstructure of the Cu–Ti–Ni–Mg–Ce alloy deformed at 750 °C with a strain rate of 0.001 s^{-1} . It can be seen from Figure 11a that the movement of dislocations is often hindered by multiple precipitation phases, forming large entangled dislocations and precipitation phases. It can be seen from Figure 11b that a part of the precipitated phase exists on the subgrain boundary, thereby pinning the subgrain boundary, which can effectively hinder the migration of the subgrain boundary during hot deformation. Figure 11c is the corresponding SADP of the precipitate in the blue circle in Figure 11b. According to the SADP calibration results, it is determined that the precipitated phase is CuNi_2Ti . Figure 11d is another large-size phase, and Figure 11e is the HRTEM of the yellow circled area in Figure 11d. Figure 11f is the fast Fourier transform (FFT) corresponding to the precipitation. According to the calibration results in Figure 11f, it is determined that the precipitation phase is Cu_4Ti , the crystal plane spacing $d_{(102)} = 0.37$ nm, the zone axis of Cu_4Ti is $[0\bar{1}0]_{\text{Cu}_4\text{Ti}}$, and the lattice parameters are $a = 4.53$ nm, $b = 4.53$ nm, and $c = 12.93$ nm.

The number of precipitates in the Cu–Ti–Ni–Mg–Ce alloy is higher and their size is smaller than the Cu–Ti–Ni–Mg alloy. According to the above analysis, the addition of Ce promotes the precipitation of CuNi_2Ti . Due to the interaction between dislocations and precipitates, the precipitate is nailed to dislocation and subgrain boundary, which hinders dislocation movement, thus improving the flow stress and activation energy of the Cu–Ti–Ni–Mg alloy.

4. Conclusions

The hot deformation tests of the Cu–Ti–Ni–Mg and Cu–Ti–Ni–Mg–Ce alloys were investigated at temperatures ranging from 550 to 950 °C and strain rates ranging from 0.001 to 10 s^{-1} . The effects of Ce addition on the microstructure evolution were discussed. Through the comparison and analysis of the experimental results, the following conclusions can be drawn: 1) The addition of Ce increases the flow stress of the Cu–Ti–Ni–Mg alloy while increasing the activation energy of

the alloy from 344.02 to 389.87 kJ mol^{-1} . The addition of Ce improves the deformation resistance during hot deformation. 2) The addition of Ce increases the misorientation angle, reduces the dislocation density and texture strength, and promotes the dynamic recrystallization of the alloy. When the temperature was increased from 750 to 850 °C, the main fiber texture of Cu–Ti–Ni–Mg changed from $\langle 110 \rangle \| X$ and $\langle 111 \rangle \| X$ to $\langle 100 \rangle \| X$. The main fiber texture of Cu–Ti–Ni–Mg–Ce alloy changed from $\langle 100 \rangle \| X$ and $\langle 111 \rangle \| X$ to $\langle 100 \rangle \| X$ and $\langle 110 \rangle \| X$. 3) The processing maps of the Cu–Ti–Ni–Mg and Cu–Ti–Ni–Mg–Ce alloys were established. The optimal processing domain for the Cu–Ti–Ni–Mg alloy is 825–950 °C and 0.012 – 0.162 s^{-1} strain rate, and the optimal processing domain for the Cu–Ti–Ni–Mg–Ce alloy is 725–950 °C and 0.015 – 0.185 s^{-1} strain rate. The addition of Ce expands the optimal processing domain of the Cu–Ti–Ni–Mg alloy, making the Cu–Ti–Ni–Mg alloy more suitable for processing. 4) CuNi_2Ti precipitation was found in both Cu–Ti–Ni–Mg and Cu–Ti–Ni–Mg–Ce alloys, while Cu_4Ti precipitation was found in the Cu–Ti–Ni–Mg–Ce alloy. The Cu–Ti–Ni–Mg–Ce alloy has more and finer precipitates. Thus, promoting precipitation hinders the movement of dislocations and improves the properties of the alloy.

Acknowledgements

This research was supported by the National Natural Science Foundation of China (grant no. 52071134), the Program for Innovative Research Team at the University of Henan Province (grant no. 22IRTSTHN001), China Postdoctoral Science Foundation (grant nos. 2020M682316 and 2021T140779), and Outstanding Talents Innovation Fund of the Henan Province (grant no. ZYQR201912164).

Conflict of Interest

The authors declare no conflict of interest.

Data Availability Statement

Research data are not shared.

Keywords

Cu–Ti–Ni–Mg and Cu–Ti–Ni–Mg–Ce alloys, flow stresses, hot deformation, microstructure evolution, texture

Received: December 29, 2022

Revised: March 3, 2023

Published online: March 27, 2023

- [1] Y. F. Geng, X. Li, Y. Zhang, Y. L. Jia, H. L. Zhou, B. H. Tian, Y. Liu, A. A. Volinsky, X. H. Zhang, K. X. Song, P. Liu, X. H. Chen, *Vacuum* **2020**, *177*, 109376.
- [2] Y. D. Li, B. B. Yang, P. Zhang, Y. Nie, X. B. Yuan, Q. Lei, Y. P. Li, *Mater. Today Commun.* **2021**, *27*, 102266.
- [3] Q. Lei, Z. Li, M. P. Wang, L. Zhang, S. Gong, Z. Xiao, Z. Y. Pan, *J. Alloys Compd.* **2011**, *509*, 3617.

- [4] K. X. Song, Y. F. Geng, Y. J. Ban, Y. Zhang, Z. Li, X. J. Mi, J. Cao, Y. J. Zhou, X. B. Zhang, *J. Mater. Sci. Technol.* **2021**, 79, 75.
- [5] X. Wang, Z. Xiao, W. T. Qiu, Z. Li, F. Liu, *Mater. Sci. Eng., A* **2020**, 803, 140510.
- [6] J. Chalou, J. D. Guérin, L. Dubar, A. Dubois, E. S. Puchi-Cabrera, *Mater. Sci. Eng., A* **2016**, 667, 77.
- [7] R. Markandeya, S. Nagarjuna, D. S. Sarma, *Mater. Sci. Eng., A* **2005**, 404, 305.
- [8] R. Markandeya, S. Nagarjuna, D. S. Sarma, *Mater. Charact.* **2005**, 54, 360.
- [9] F. L. Wang, Y. P. Li, K. Wakoh, Y. Koizumi, A. Chiba, *Mater. Des.* **2014**, 61, 70.
- [10] R. Markandeya, S. Nagarjuna, D. S. Sarma, *Mater. Charact.* **2006**, 57, 348.
- [11] S. Nagarjuna, U. S. Babu, *Mater. Sci. Eng., A* **2008**, 491, 331.
- [12] R. Markandeya, S. Nagarjuna, D. S. Sarma, *Mater. Sci. Eng., A* **2004**, 371, 291.
- [13] X. Wang, L. Zhou, Z. Xiao, W. T. Wang, *Trans. Nonferrous Met. Soc.* **2020**, 30, 2737.
- [14] T. J. Konno, R. Nishio, S. Semboshi, T. Ohsuna, E. Okunishi, *J. Mater. Sci.* **2008**, 43, 3761.
- [15] R. Markandeya, S. Nagarjuna, D. V. V. Satyanarayana, D. S. Sarma, *Mater. Sci. Eng., A* **2006**, 428, 233.
- [16] V. Lebreton, D. Pachoutinski, Y. Bienvenu, *Mater. Sci. Eng., A* **2009**, 508, 83.
- [17] J. Liu, X. H. Wang, Q. N. Ran, G. Zhao, X. X. Zhu, *Trans. Nonferrous Met. Soc. China.* **2016**, 26, 3183.
- [18] J. Liu, X. H. Wang, T. T. Guo, J. T. Zou, X. H. Yang, *Rare Met. Mater. Eng.* **2016**, 45, 1162.
- [19] B. Rouxel, C. Cayron, J. Bornand, P. Sanders, R. E. Logé, *Mater. Des.* **2022**, 213, 110340.
- [20] K. Maki, Y. Ito, H. Matsunaga, H. Mori, *Scr. Mater.* **2013**, 68, 777.
- [21] Y. J. Ban, Y. Zhang, B. H. Tian, Y. L. Jia, K. X. Song, X. Li, M. Zhou, Y. Liu, A. A. Volinsky, *Materials* **2020**, 13, 3186.
- [22] N. Stanford, D. Atwell, A. Beer, C. Davies, M. R. Barnett, *Scr. Mater.* **2008**, 59, 772.
- [23] N. Stanford, *Mater. Sci. Eng., A* **2010**, 527, 2669.
- [24] Y. Zhang, Z. Chai, A. A. Volinsky, B. H. Tian, H. L. Sun, P. Liu, Y. Liu, *Mater. Sci. Eng., A* **2016**, 662, 320.
- [25] Y. Q. Ning, X. Luo, H. Q. Liang, H. Z. Guo, J. L. Zhang, K. Tan, *Mater. Sci. Eng., A* **2015**, 635, 77.
- [26] J. Yi, Y. Jia, Y. Y. Zhao, Z. Xiao, K. J. He, Q. Wang, M. P. Wang, Z. Li, *Acta Mater.* **2019**, 166, 261.
- [27] A. S. H. Kabir, M. Sanjari, J. Su, I. H. Jung, S. Yue, *Mater. Sci. Eng., A* **2014**, 616, 252.
- [28] B. J. Wang, Y. Zhang, B. H. Tian, J. C. An, A. A. Volinsky, H. L. Sun, Y. Liu, K. X. Song, *Vacuum* **2018**, 155, 594.
- [29] S. L. Tang, M. Zhou, X. Li, Y. Zhang, D. Y. Xu, Y. Z. Zhang, B. H. Hong, Y. L. Jia, Y. Liu, A. A. Volinsky, *Mater. Today Commun.* **2022**, 31, 103771.
- [30] T. Wei, Y. D. Wang, Z. H. Tang, S. F. Xiao, *Mater. Today Commun.* **2021**, 7, 102471.
- [31] C. M. Sellars, W. J. McTegart, *Acta Metall.* **1966**, 14, 1136.
- [32] H. Mirzadeh, *Mater. Des.* **2015**, 65, 80.
- [33] H. Khodashenas, H. Mirzadeh, M. Malekan, M. Emamy, *Vacuum* **2019**, 170, 108970.
- [34] K. Edalati, Z. Horita, *Scr. Mater.* **2011**, 64, 161.
- [35] J. Liu, X. H. Wang, J. T. Liu, Y. F. Liu, H. G. Li, C. Wang, *J. Alloys Compd.* **2019**, 782, 224.
- [36] I. S. Batra, G. K. Dey, U. D. Kulkarni, *J. Nucl. Mater.* **2001**, 299, 91.
- [37] Q. Lei, Z. Li, J. Wang, S. Li, L. Zhang, Q. Y. Zhang, *J. Mater. Sci.* **2012**, 47, 6034.
- [38] F. Bittner, S. Yin, A. Kauffmann, J. Freudenberger, H. Klauß, G. Korpala, R. Kawalla, W. Schillinger, L. Schultz, *Mater. Sci. Eng., A* **2014**, 597, 139.
- [39] P. F. Yang, M. Zhou, Y. Zhang, Y. L. Jia, B. H. Tian, Y. Liu, X. Li, A. A. Volinsky, *Mater. Charact.* **2021**, 181, 111502.
- [40] W. J. He, A. Chapuis, X. Chen, Q. Liu, *Mater. Sci. Eng., A* **2018**, 734, 364.
- [41] Y. S. Wu, X. Z. Qin, C. S. Wang, L. Z. Zhou, *Mater. Sci. Eng., A* **2019**, 768, 138454.
- [42] X. L. Ma, C. X. Huang, J. Moering, M. Ruppert, H. W. Hoppel, M. Goken, J. Narayan, Y. Zhu, *Acta Mater.* **2016**, 116, 43.
- [43] Y. Zhang, H. L. Sun, A. A. Volinsky, B. J. Wang, B. H. Tian, Z. Chai, Y. Liu, K. X. Song, *Adv. Eng. Mater.* **2017**, 19, 1700197.